

On the Role of Yttrium in Alumina Formers: Comparative Oxidation Behavior of (Ni–Cr–Al)- and (Ni–Cr–Al–Y)-Based Alloys

H. M. Tawancy¹

Received: 2 July 2016/Revised: 6 August 2016/Published online: 13 August 2016
© Springer Science+Business Media New York 2016

Abstract It is shown that the addition of Y to an alloy based upon the Ni–Cr–Al system slightly reduces the growth rate of Al_2O_3 scale during isothermal oxidation in air at temperatures in the range of 950–1150 °C. However, Y segregation at grain boundaries of the oxide is found to refine its grain structure down to the nanoscale with improved mechanical strength as compared to the Y-free alloy. It is concluded that Y can have the effect of decelerating the kinetics of diffusion processes leading to grain growth of the oxide.

Keywords Al_2O_3 · Yttrium · Segregation · Ni–Cr–Al system · Electron microscopy

Introduction

Increasing the efficiency of energy conversion systems and effectively capturing carbon waste in the form of CO_2 are largely dependent upon the use of structural materials capable of resisting various corrosive environments [1]. For example, materials for shift reactor applications in carbon capture systems can be exposed to highly carburizing environments [2]. A recent study has shown that a one-to-one correspondence exists between the resistance to oxidation and resistance to carburization of selected high-temperature alloys and that alloys environmentally protected by Al_2O_3 -based scale offer the highest resistance [3]. Among these alloys is the solid-solution-strengthened Haynes alloy 214, which is based upon the Ni–Cr–Al–Y system [4].

✉ H. M. Tawancy
tawancy@kfupm.edu.sa

¹ Center for Engineering Research, Research Institute, King Fahd University of Petroleum and Minerals, P.O. Box 1639, Dhahran 31261, Saudi Arabia

Although it has long been known that Y can significantly improve the protective nature of Al_2O_3 -based scale [5], the underlying mechanism is still subject to debate. Several studies have shown that the growth of Al_2O_3 occurs by short-circuit diffusion of both O [6] and Al [7] along grain boundaries with diffusion of O predominating in many systems [8, 9]. An earlier study of alloy 214 has shown that Y segregates at the grain boundaries of the protective Al_2O_3 scale adhered to the alloy substrate [10] similar to other Al_2O_3 -forming alloys [11–14]. However, there have been conflicting reports regarding the mechanism by which Y segregation improves the oxidation resistance. Some studies suggest that Y segregation at the grain boundaries of Al_2O_3 scale tends to block the diffusion of both O and Al and, therefore, decelerates the kinetics of oxide growth [15, 16]. Recently, a new approach based upon the electronic structure of Al_2O_3 has been advanced to explain its growth on various alloy systems from the first principles [17–19]. It is predicted that grain boundary diffusion of both Al and O are involved in Al_2O_3 growth consistent with earlier studies. However, the new approach predicts that deceleration of oxide growth by the addition of active elements such as Y and Hf stems from the modification of the near-band gap edge grain boundary defects contrary to earlier suggestions that the effect is related to blocking grain boundary diffusion. It is noted here that the experiment shows that active elements slightly reduce the oxide growth rate of Al_2O_3 on Ni–Cr–Al alloys and have no measurable effect in the case of Fe–Cr–Al alloys [12, 20], and that the major beneficial effect stems from improving the oxide adhesion to the substrate [9, 12, 16, 21].

A number of studies of the oxidation behavior of alloy 214 have focused on the transition from slow oxidation to breakaway oxidation in thin sections of material (foils ranging from 155 to 300 μm in thickness) where the stage of breakaway oxidation occurs prior to substantial oxide spallation [22–24]. It is found that upon depletion of the Al content of the alloy due to the continued formation and spallation of the Al_2O_3 scale, a protective layer of chromia is developed, which can extend the useful life of the alloy in several applications. Another study has demonstrated the high resistance of alloy 214 toward spallation of the Al_2O_3 scale during cyclic oxidation, which has been attributed to the improved oxide adhesion provided by the presence of Y [25]. Also, it has been shown that the Al_2O_3 scale developed by alloy 214 retards the ingress of carbon, and therefore the alloy is characterized by high resistance to carburizing environments [3]. A recent study of the oxidation kinetics of porous alloy 214 at temperatures in the range of 850–1000 $^\circ\text{C}$ has revealed an initial quasi-parabolic stage with more rapid kinetics followed by a second parabolic stage with slower kinetics [26]. It is therefore apparent that most of the previous studies have been devoted to demonstrate the advantages offered by alloy 214 as a wrought oxidation-resistant alloy primarily protected by Al_2O_3 scale. In the meantime, there is still a controversy surrounding the mechanism underlying the beneficial effect resulting from Y segregation at the oxide grain boundaries as pointed out earlier. This requires, at least partially, a systematic study devoted to comparing the oxidation behavior of alloy 214 with a Y-free version of the alloy. To fill that gap, the present investigation has been undertaken with a particular emphasis on the effect of Y on the oxidation kinetics

and microstructure of the protective layer of Al_2O_3 down to the scale of transmission electron microscopy.

Experimental Procedures

Samples of alloy 214 were obtained in the form of sheets with 1.5 mm thickness. A Y-free version of the alloy was prepared by standard techniques of vacuum induction melting and electroslag remelting followed by forging, hot rolling, and finally cold rolling into sheets 1.5 mm in thickness. Specimens with the dimensions of $30 \times 30 \times 1.5$ mm were machined from the sheets and solution annealed at 1095°C for 15 min under argon atmosphere followed by water quenching. Inductively coupled plasma atomic emission spectroscopy was used to determine the chemical compositions of the two alloys with the exception of C content, which was measured by combustion calorimetry. The grain structure of each alloy in the annealed condition was revealed by etching in 10 % aqueous solution of oxalic acid, and the initial distribution of Y in alloy 214 was determined by Auger electron spectroscopy. Isothermal oxidation tests were carried out in air at 950, 1000, 1050, 1100, and 1150°C to determine the oxidation kinetics using thermogravimetric unit for continuous weight measurement. Scanning electron microscopy (SEM) and energy-dispersive spectroscopy (EDS) were used to analyze the morphology and composition of the oxide scales. Additional specimens for 100-h isothermal oxidation tests at 1150°C were first reduced to about 0.5 mm in thickness and then 3-mm-diameter disks were punched and heat treated as described above. These specimens were used to characterize the microstructure of the oxide scale near the oxide–metal interface by transmission electron microscopy (TEM), electron diffraction, and EDS. Thin foils for TEM were prepared from the oxidized 3-mm-diameter disks using the combination of electropolishing and ion beam milling [13, 27]. The specimens were first perforated by the jet polishing technique on one side in a solution consisting of 30 pct. nitric acid in methanol to dissolve the metal near the oxide–metal interface. Final thinning was carried out by focused ion beam milling. All foils were examined at an accelerating voltage of 200 keV. Henceforth, the Y-free version of alloy 214 is referred to as alloy 214-Y.

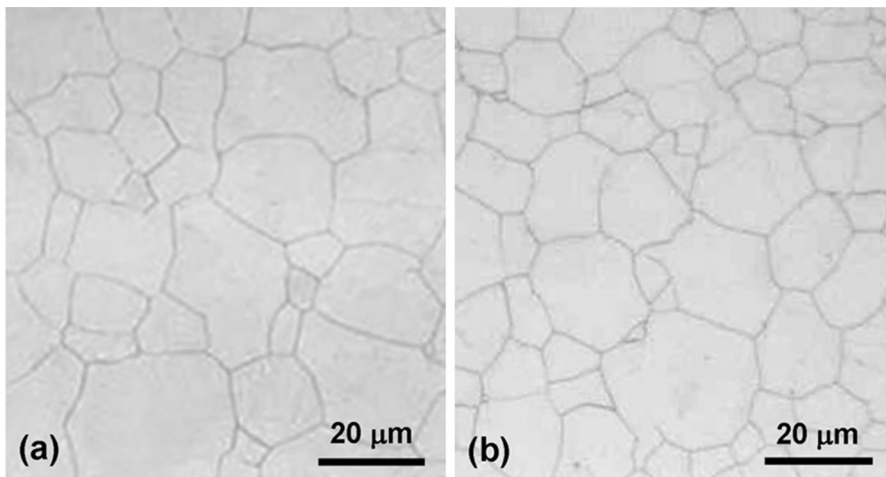
Results and Discussion

Initial Microstructures

Table 1 summarizes the chemical compositions of the two alloys investigated. As shown in Fig. 1a, b, the grain structures of the two alloys in the annealed condition are quite similar. Figure 2 summarizes the results of analyzing the initial distribution of Y in alloy 214 by Auger electron spectroscopy. An Auger spectrum derived from the outermost surface layer of alloy 214 is shown in Fig. 2a where a characteristic Y peak is observed. It is noted that on an atomic scale, the concentration of Y in alloy 214 is 0.006 %, which is far below the 0.1 at.% detection

Table 1 Chemical compositions in wt %

Element	Alloy 214	Alloy 214-Y
Ni	75.54	76.30
Cr	16.83	16.54
Fe	2.30	2.67
Mn	0.20	0.15
Si	0.09	0.13
Al	4.57	4.82
C	0.04	0.03
B	0.01	0.01
Y	0.01	0.01

**Fig. 1** Optical micrographs illustrating the initial microstructures of the alloys investigated in the annealed condition: **a** alloy 214-Y and **b** alloy 214

limit of Auger electron spectroscopy [28] indicating the tendency of Y to segregate at the free surface. This is further confirmed by the data of Fig. 2b showing Y depth profile. It is observed that Y is segregated within a surface layer about 1.6 nm in thickness. As shown later, Y remains close to the alloy's surface during high-temperature oxidation.

Oxidation kinetics

Figure 3 shows a parabolic plot of the mass gain versus the square root of time at 950 and 1150 °C using the relationship $x^2 = kt$, where x is the mass gain per unit area, k is the reaction rate constant at a given temperature, and t is the exposure time. It is observed that the addition of Y slightly reduces the oxide growth rate consistent with the results of earlier studies of other Al_2O_3 -forming Ni–Cr–Al-based alloys [12, 20]. As shown in Fig. 3, both alloys exhibit an initial stage of oxidation

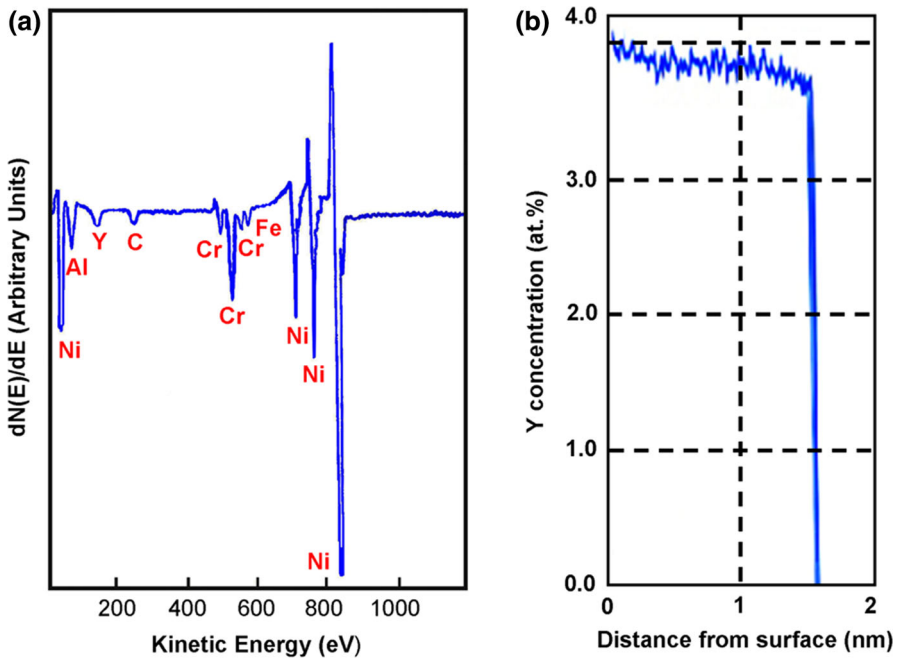


Fig. 2 Segregation of Y at the free surface of alloy 214 in the annealed condition: **a** Auger spectrum derived from the surface and **b** Y depth profile (Y concentration vs. distance from the free surface)

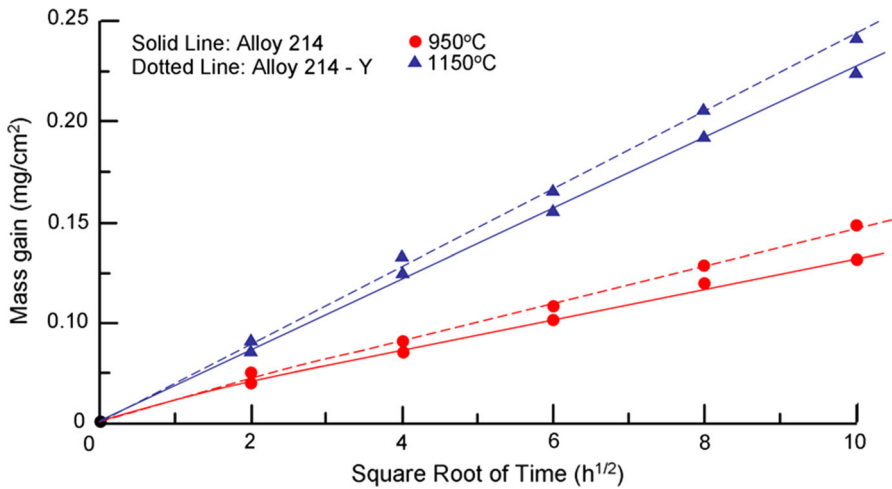


Fig. 3 Parabolic plots of the mass gain versus square root of time illustrating the kinetics of isothermal oxidation in air of alloys 214 and 214-Y at 950 and 1150 °C

with relatively rapid kinetics followed by a second stage of slower kinetics at 950 °C. Although the second stage closely follows the parabolic rate law, the first stage exhibits some deviation indicating the occurrence of an initial stage of

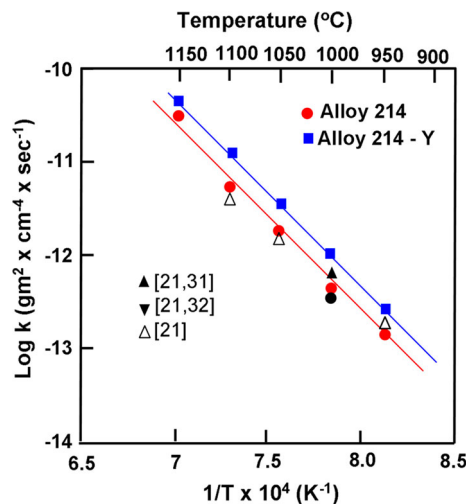
transient oxidation. However, at 1150 °C, it can be seen that the deviation from parabolic behavior has diminished. Evidently, it takes longer exposure time at lower temperatures for the kinetics to follow the parabolic rate law, which is an expected behavior of the diffusion-controlled oxidation reactions [29]. It is recalled that in a study of the oxidation kinetics of porous alloy 214, an initial stage of transient oxidation has been observed in the range of 850–1000 °C [26].

Figure 4 shows the functional dependence of the reaction rate constant k on temperature during isothermal oxidation in air at temperatures in the range of 950–1150 °C as determined from the parabolic relationship $x^2 = kt$ and the Arrhenius rate equation $k = k_0 \exp(-Q/RT)$, where k_0 is a constant, Q is the activation energy of the oxidation reaction, R is the universal gas constant, and T is the temperature in degrees Kelvin. Although the addition of Y slightly reduces the oxide growth rate, it is observed to have no measurable effect on the activation energy, which is estimated to be about 396 kJ/mol. This activation energy is to be compared with a value of 382 kJ/mol reported for other (Ni–Cr–Al)-based alloys [30]. For comparative purposes, Fig. 4 also shows that the present kinetic rates are comparable to those of other Al_2O_3 -forming alloys such as Ni–16Cr–6Al [21, 31], Ni–13Al–0.5Y [21, 32], and Ni–10Cr–5Al–0.5Y [21, 33].

Evolution of the oxide scale

Both alloys are found to exhibit similar morphological features of the surface oxide layers on the scale of SEM. For example, Fig. 5 shows secondary electron SEM images illustrating the gross morphological features of the surface scale developed by each alloy on the same area within the first 1 h of exposure in air at 1150 °C. It is observed that each alloy develops a multilayer oxide with an outermost layer of NiO. Figure 6 shows the morphology of NiO formed on both alloys after 15 min of exposure at 1150 °C at high magnification. As an example, Fig. 7 shows the

Fig. 4 Functional dependence of reaction rate k on temperature for alloys 214 and 214-Y; for comparative purposes, respective data for other Al_2O_3 -forming alloys are also shown



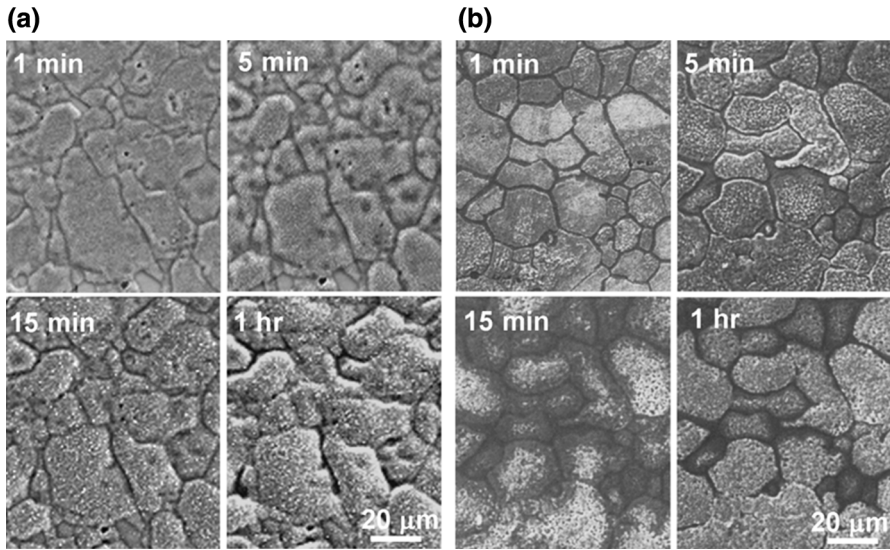


Fig. 5 Secondary electron SEM images illustrating the effect of exposure time at 1150 °C on the morphology of surface oxide developed by alloys 214-Y and 214 during the stage of primary oxidation; **a** alloy 214-Y and **b** alloy 214

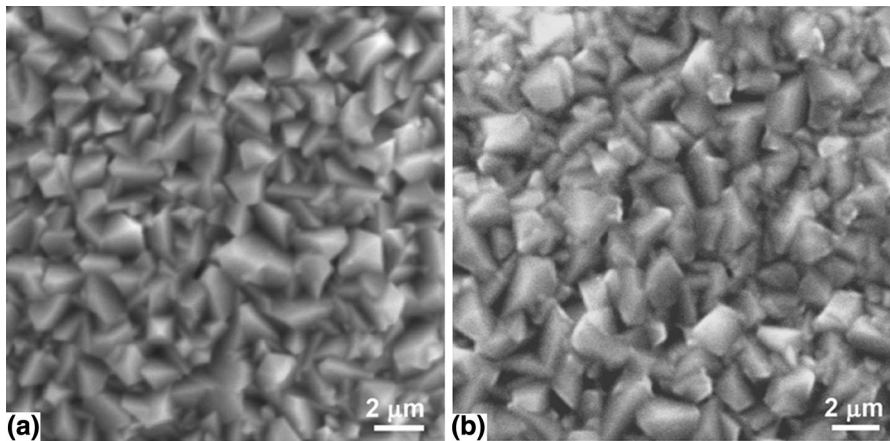


Fig. 6 Secondary electron SEM images illustrating the morphology of the outermost layer of NiO developed by the two alloys after 15 min of exposure at 1150 °C: **a** alloy 214-Y and **b** alloy 214

elemental compositions of the various oxide layers developed by alloy 214 after 15 min of exposure at 1150 °C. It is observed that the outermost layer of NiO is followed by a layer with major elemental constituents of Ni, Al, Cr, and O expected to be a spinel of the type $\text{Ni}(\text{Al},\text{Cr})_2\text{O}_4$ followed by an inner layer of Cr-rich oxide consistent with Cr_2O_3 . Evidently, at that early stage of oxidation, the volume fraction of Al_2O_3 has been too small to be detected in agreement with a mechanism

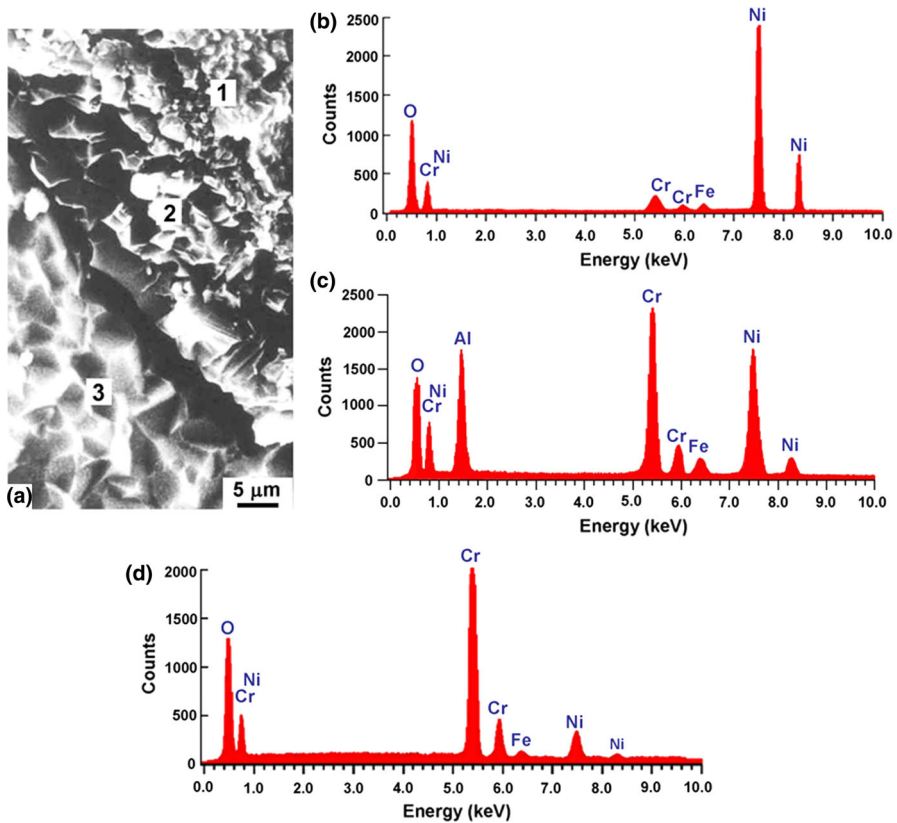


Fig. 7 An example illustrating the elemental compositions of the surface oxides developed by alloy 214 after 15 min of exposure at 1150 °C. **a** Secondary electron SEM image illustrating the multilayer oxide. **b**, **c**, and **d** EDS spectra illustrating the elemental compositions of oxide layers marked 1, 2, and 3, respectively, in **(a)**

proposed to explain the isothermal oxidation mechanism of Ni–16Cr–6Al alloy [34].

Figure 8 shows the x-ray diffraction patterns derived from the surface of each alloy after 24 h of exposure at 1150 °C. All observed Bragg diffraction maxima are consistently indexed in terms of the crystal structures of four oxide phases: (i) NiO (cubic; $a = 0.42$ nm), (ii) spinel isomorphous with NiCr_2O_4 (cubic; $a = 0.82$ nm), (iii) $-\text{Cr}_2\text{O}_3$ (hexagonal; $a = 0.49$ nm, $c = 1.36$ nm), and (iv) $-\text{Al}_2\text{O}_3$ (hexagonal; $a = 0.48$ nm, $c = 1.30$ nm).

The above observations indicate that the gross oxidation behavior of alloy 214 and alloy 214–Y down to the scale of SEM are quite similar. However, a significant difference in the microstructure of the Al_2O_3 layer formed in contact with the alloy substrate is observed on the finer scale of TEM as demonstrated below.

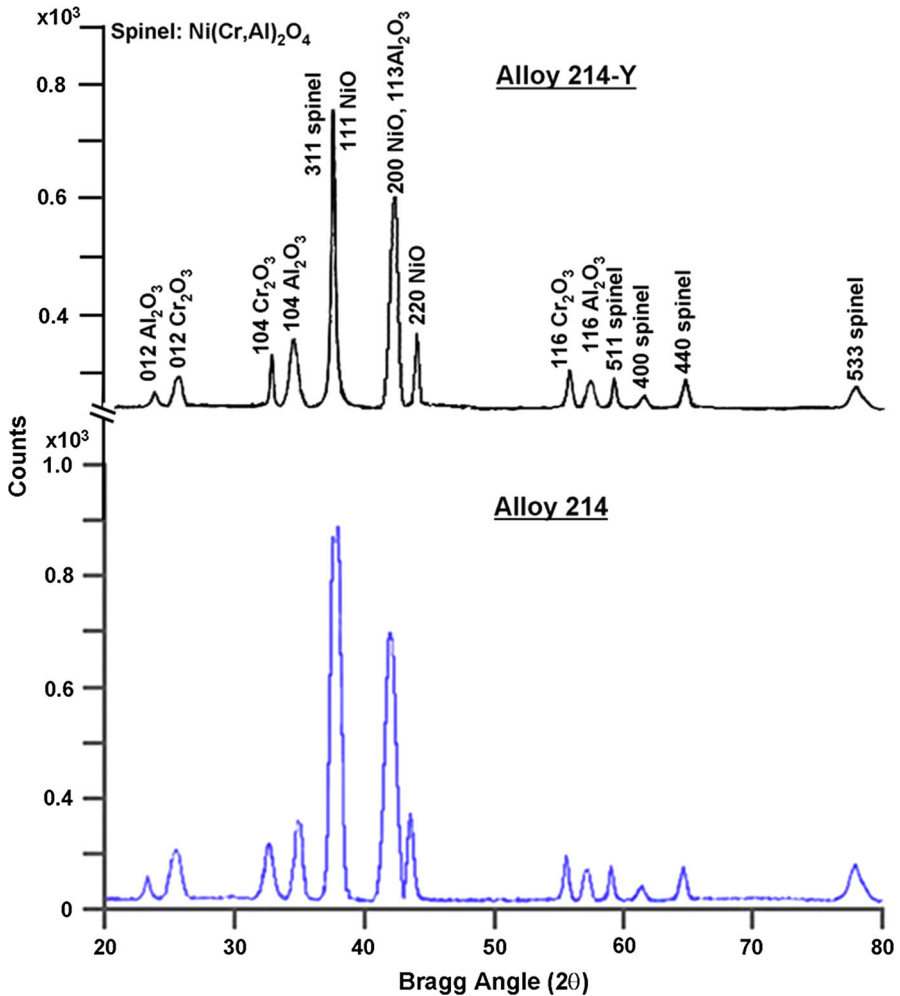


Fig. 8 Comparative x-ray diffraction patterns derived from the oxides developed by the two alloys investigated after 24 h of exposure at 1150 °C (steady-state oxidation): **a** alloy 214-Y and **b** alloy 214

Effect of Y on the microstructure of Al_2O_3

Figure 9 illustrates the difference in the microstructure of Al_2O_3 layer formed near the oxide–metal interface of each alloy on the scale of TEM. Figure 8a shows a bright-field TEM image illustrating the grain structure of Al_2O_3 formed near the oxide–metal interface of alloy 214-Y. The inset shows the microdiffraction pattern derived from the grain marked (x) consistent with the hexagonal structure of Al_2O_3 in [1–100] orientation. Addition of Y is found to refine the grain structure down to the nanoscale as demonstrated in the bright-field TEM image of Fig. 8b with the corresponding selected-area ring diffraction pattern in the inset and indexed in terms of the hexagonal structure of Al_2O_3 . The corresponding elemental composition is

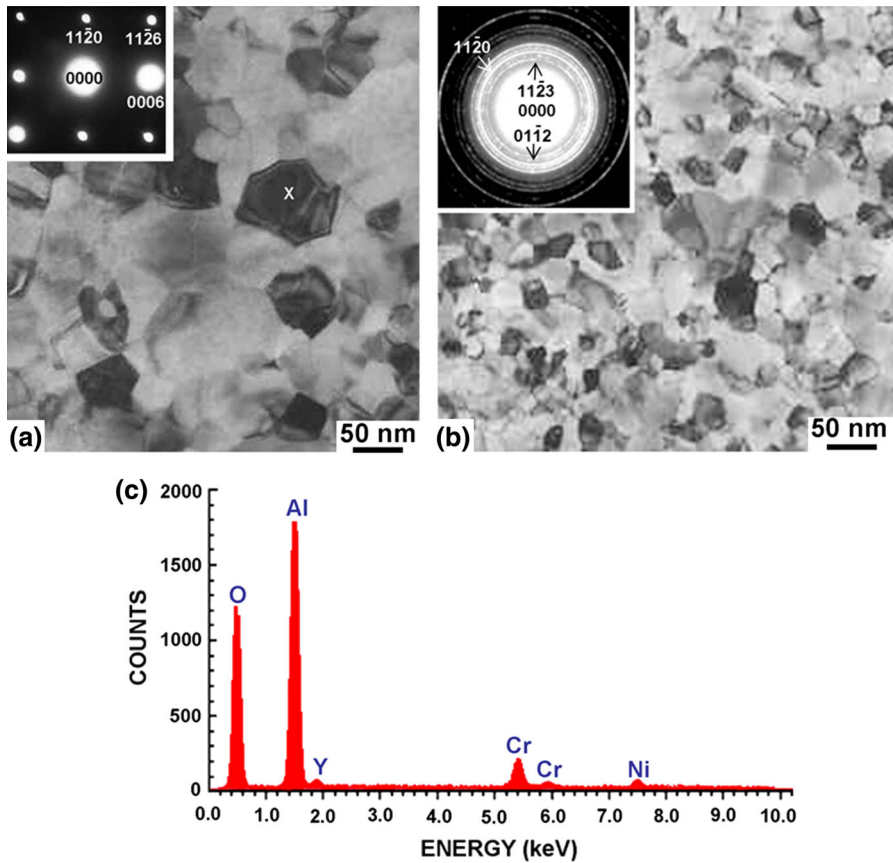


Fig. 9 Effect of Y on the microstructure of Al_2O_3 layer formed near the oxide–metal interface of each alloy after 100 h of exposure at 1150 °C. **a** Bright-field TEM image illustrating the grain structure of the oxide developed by alloy 214-Y; the *inset* shows the microdiffraction pattern derived from the grain marked (x) and consistent with the hexagonal structure of $\alpha\text{-Al}_2\text{O}_3$ in [1–100] orientation. **b** Bright-field TEM image illustrating the grain structure of the oxide developed by alloy 214; the *inset* is corresponding selected-area ring diffraction pattern consistent with the hexagonal structure of $\alpha\text{-Al}_2\text{O}_3$. **c** EDS spectrum showing the elemental composition of the oxide in (b)

shown in the EDS spectrum of Fig. 8c. As can be seen, the major elemental constituents of the oxide are Al and O with smaller concentrations of Cr and Ni, and a minor concentration of Y distributed as described below.

The distribution of elemental Y throughout the grain structure of Al_2O_3 developed by alloy 214 near the oxide–metal interface is illustrated in the bright-field TEM image of Fig. 10a and the corresponding concentration profile of Y shown in Fig. 10b. It is observed that as the oxide grain boundary is approached, the Y concentration increases reaching a maximum value at the boundary, which amounts to more than 3-fold that in the matrix. This observation can lead to the conclusion that the oxide grain structure developed by alloy 214 has been refined down to the nanoscale by segregation of Y at the grain boundaries.

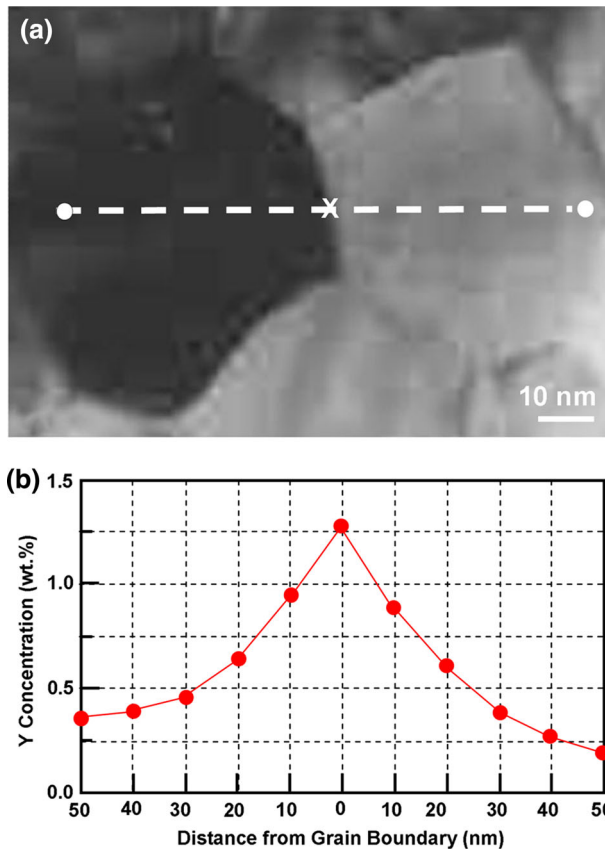


Fig. 10 Segregation of Y at the grain boundaries of Al_2O_3 developed by alloy 214 after 100 h of exposure at 1150 °C. **a** Bright-field TEM image showing the grain structure of the oxide. **b** Corresponding concentration profile of Y across the grain boundary in (a)

A nanostructured oxide scale such as that observed in Fig. 9b (alloy 214) is expected to have improved high-temperature mechanical strength in comparison with the coarse grain structure shown in Fig. 9a (alloy 214-Y) [35, 36]. It is evident that Y reduces the mobility of grain boundaries and increases the resistance to grain growth, which is generally known to be controlled by grain boundary diffusion [37, 38]. Therefore, the role of Y in decelerating the kinetics of grain boundary diffusion cannot be totally discounted.

Conclusion

It is concluded from this study that Y in the (Ni–Cr–Al)-based alloy 214 has a slight effect on the growth rate of Al_2O_3 during high-temperature oxidation. However, maintaining a nanostructured oxide by Y segregation at grain boundaries indicates that Y reduces the mobility of grain boundaries at elevated temperatures, which can

be correlated with the decelerating kinetics of diffusional processes leading to grain growth. In the meantime, the nanostructured oxide is expected to have improved high-temperature mechanical strength.

Acknowledgments The author is grateful for the continued support provided by King Fahd University of Petroleum and Minerals.

References

1. E. Opila, *The Electrochemical Society Interface* **22**, 69 (2013).
2. B. A. Billingham, C. H. Lee, L. Smith, M. Haines, S. R. James, B. K. W. Goh, K. Dvorak, L. Robinson, C. J. Davis and D. P. Solorio, *Energy Procedia* **4**, 2020 (2011).
3. H. M. Tawancy, *Oxidation of Metals* **83**, 167 (2015).
4. R. B. Herchenroeder, G. Y. Lai and K. V. Rao, *Journal of Metals* **35**, 16 (1983).
5. D. P. Whittle and J. Stringer, *Philosophical Transactions of the Royal Society* **A295**, 309 (1980).
6. K. P. R. Reddy, J. L. Smialek and A. R. Cooper, *Oxidation of Metals* **17**, 429 (1982).
7. E. W. A. Young and J. H. W. de Wit, *Oxidation of Metals* **26**, 351 (1986).
8. J. L. Smialek, *Corrosion Science* **91**, 281 (2015).
9. F. H. Stott, in *The role of active elements in the oxidation behavior of high temperature metals and alloys*, ed. E. Lang (Elsevier Applied Science, London, 1989), p. 3.
10. H. M. Tawancy, *Metallurgical Transactions A* **22A**, 1463 (1991).
11. L. V. Ramanathan, *Corrosion Science* **35**, 871 (1993).
12. T. A. Ramanarayanan, R. Ayer, R. Petkovic-Luton and D. P. Leta, *Oxidation of Metals* **29**, 445 (1988).
13. T. A. Ramanarayanan, M. Raghavan and R. Petkovic-Luton, *Oxidation of Metals* **22**, 83 (1984).
14. T. A. Ramanarayanan, M. Raghavan and R. Petkovic-Luton, *Journal of the Electrochemical Society* **131**, 923 (1984).
15. J. Stringer, *Materials Science and Engineering A* **120**, 129 (1989).
16. A. M. Huntz, in *The Role of Active Elements in the Oxidation Behavior of High Temperature Metals and Alloys*, ed. E. Lang (Elsevier Applied Science, London, 1989), p. 81.
17. A. H. Heuer, M. Z. Zahiri, H. Guhl, M. Foulkes, B. Gleeson, T. Nakagawa, Y. Ikuhara and M. W. Finnis, *Journal of the American Ceramic Society* **99**, 733 (2016).
18. A. H. Heuer, T. Nakagawa, M. Z. Azar, D. B. Hovis, J. L. Smialek, B. Gleeson, N. D. M. Hine, H. Guhl, H. S. Lee, P. Tangney, W. M. C. Foulkes and W. M. Finnis, *Acta Materialia* **61**, 6670 (2013).
19. A. H. Heuer, D. B. Hovis, J. L. Smialek and B. Gleeson, *Journal of the American Ceramic Society* **94**, s146 (2011).
20. R. Prescott and M. J. Graham, *Oxidation of Metals* **38**, 233 (1992).
21. H. Hindam and D. P. Whittle, *Oxidation of Metals* **18**, 245 (1982).
22. A. Chyrkin, N. Mortazavi, M. Halvarsson, D. Gruner and W. J. Quadackers, *Corrosion Science* **98**, 688 (2015).
23. D. J. Young, A. Chyrkin, J. He, D. Gruner and W. J. Quadackers, *Oxidation of Metals* **79**, 405 (2013).
24. V. P. Deodeshmukh, *Oxidation of Metals* **79**, 567 (2013).
25. V. P. Deodeshmukh and S. K. Srivastava, *Superalloys. In The minerals, metals and materials society*, eds. R. C. Reed, K. A. Green and P. Carron (Warrendale, Pennsylvania, 2008), p. 689.
26. Y. Wang, Y. Liu, H. Tang and W. Li, *Materials Characterization* **107**, 283 (2015).
27. P. J. Goodhew, J. Humphreys and R. Beanland, *Electron microscopy and analysis*, 3rd ed, (Taylor and Francis, New York, 2002).
28. D. R. Vij, *Handbook of applied solid state spectroscopy*, (Springer, New York, 2006).
29. E. A. Gulbransen and K. F. Andrew, *Journal of the Electrochemical Society* **101**, 128 (1954).
30. M. W. Brumm and H. J. Grabke, *Corrosion Science* **33**, 1677 (1992).
31. G. S. Giggins and F. S. Pettit, *Transactions of the Metallurgical Society of AIME* **245**, 2495 (1969).
32. J. D. Kuenzly and D. L. Douglass, *Oxidation of Metals* **8**, 139 (1974).
33. A. Kumar, M. Hasrallah and D. L. Douglass, *Oxidation of Metals* **8**, 227 (1974).
34. F. S. Pettit, C. S. Giggins, J. A. Goebel and E. J. Felten, in *Alloys and microstructural design*, eds. J. K. Tien and G. S. Ansell (Academic Press, New York, 1976), p. 349.

35. J. R. Nicholls and P. Hancock, in *The role of active elements in the oxidation behavior of high temperature metals and alloys*, ed. E. Lang (Elsevier, London, 1989), p. 195.
36. J. Jedlinski, in *The role of active elements in the oxidation behavior of high temperature metals and alloys*, ed. E. Lang (Elsevier, London, 1989), p. 131.
37. A. N. Aleshin, *Russian Metallurgy* **2008**, 286 (2008).
38. V. Yamakov, D. Moldovan, K. Rastogi and D. Wolf, *Acta Materialia* **54**, 4053 (2006).